

pubs.acs.org/cm Article

Developing the Na₂CaZr₂Ge₃O₁₂:Cr³⁺ Garnet Phosphor for Advanced NIR pc-LEDs in Night Vision and Bioimaging

Published as part of Chemistry of Materials virtual special issue "C. N. R. Rao at 90".

Zurong Liao, Małgorzata Sójka, Jiyou Zhong, and Jakoah Brgoch*



Cite This: Chem. Mater. 2024, 36, 4654-4663



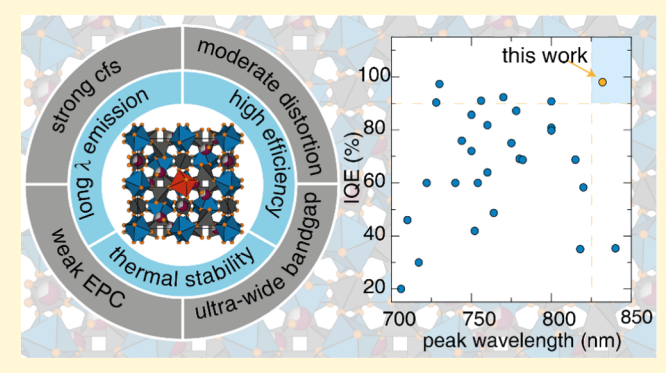
ACCESS I

III Metrics & More

Article Recommendations

s Supporting Information

ABSTRACT: Materials emitting near-infrared (NIR) light play a crucial role in the development of phosphor-converted light-emitting diodes (pc-LEDs) for applications ranging from fundamental science like spectroscopic analysis to highly applied uses like night vision and biological imaging. One class of materials that has garnered significant interest for these technical spaces is Cr^{3+} -activated garnets due to their high efficiency and ability to operate at relatively high temperatures. However, their limited emission beyond 800 nm impedes their use as optimal blue LED-pumped NIR-emitting materials. In this study, we present a new garnet-type NIR phosphor, $Na_2CaZr_2Ge_3O_{12}:Cr^{3+}$, that addresses this challenge—the material exhibits a long-wavelength emission ($\lambda_{em,max} = 832$ nm) and good thermal quenching resistance while



maintaining an excellent internal quantum efficiency (IQE = 98%). These properties are attributed to a crystal environment reconstruction, where a crystal structure distortion is coupled to a weak crystal field, which is uncommon for most rigid garnet-type phosphors. Furthermore, the fabricated NIR pc-LED devices using this material demonstrate superior performance compared with devices employing well-known efficient NIR phosphors operating in this emission range. The light source is subsequently demonstrated in applications spanning night vision, bioimaging, and nondestructive analysis. This study not only provides insights into the luminescence properties of Cr³⁺-activated garnet materials with desirable performance but also highlights the practical application of NIR-emitting garnet phosphors.

1. INTRODUCTION

Near-infrared (NIR) light spanning from 780 to 1100 nm boasts a diversity of potential applications across various domains, including nondestructive food-quality analysis, medical diagnostics and treatment, biological imaging, plant growth, security monitoring, and remote temperature and pressure monitoring, among numerous other fields. 1-6 Presently, the available NIR light sources used for such spectroscopic or imaging techniques predominantly comprise incandescent halogen lamps or direct-conversion light-emitting diodes (LEDs). Each source has distinct advantages and drawbacks. Incandescent lamps possess the ability to generate continuous light emission spanning the NIR range, but they struggle with issues of poor energy efficiency, a restricted operating lifespan, and substantial size. 7,8 LEDs, on the other hand, address the inefficiency problems compared to incandescent lamps; however, they have a narrow emission spectrum, limited output power in the NIR range, and elevated cost, which currently discourage broad industrial consideration.^{7,9} Compared with the direct-emitter NIR LED sources, NIR phosphor-converted light-emitting diodes (NIR pc-LEDs) have become a popular option by using a higher-efficiency

blue-emitting InGaN LED chip coated with a near-infrared-emitting inorganic phosphor. The phosphor absorbs the emitted blue LED radiation and down-converts the photons into the NIR region of the electromagnetic spectrum. This approach possesses distinct advantages such as the same compact size, long lifetime, and even less energy consumption compared with direct-emitting NIR LEDs. They also have the added benefit of an easily adjustable emission spectrum, including the ability to cover nearly the entire NIR region similar to the incandescent lamps using a single broad-emitting phosphor. ^{10–15} These attributes make them ideal for future integration into portable smart devices, enabling a wide array of applications.

Received: February 15, 2024
Revised: April 18, 2024
Accepted: April 23, 2024
Published: May 1, 2024





The careful selection of a broadband NIR phosphor is pivotal for optimizing the overall performance of NIR pc-LEDs. This choice impacts the device's total light output. Given that current InGaN LEDs typically operate at around \approx 423 K, it becomes necessary to prioritize the development of broadband NIR phosphors that not only provide extensive spectral coverage but also possess exceptional thermal stability. 16-18 Indeed, combination of the large Stoke shifts associated with blue light absorption and NIR emission generates intrinsic, nonradiative relaxation that acts as a local atomic-scale heat source. 19 Combined with the general heating experienced by the phosphors during overall device operation, managing thermal effects becomes critical for NIR phosphor performance. The best option today for meeting these needs are Cr3+-activated materials, owing to their efficient absorption in the blue region of the electromagnetic spectrum, aligning with the commercially produced InGaN blue-emitting LEDs, and the ability to produce tunable broadband NIR emission when incorporated into a weak octahedral crystal field. 7,8,20-22 As a result, many Cr3+-activated phosphors have emerged in recent years, with particular focus on the garnet family. Here, multiple Cr3+-activated materials have been identified, showcasing a remarkable combination of internal quantum efficiency (IQE) and exceptional thermal stability. For instance, $Gd_3Sc_{1.5}Al_{0.5}Ga_3O_{12}:Cr^{3+}$ ($\lambda_{em,max}=756$ nm) and $Ca_3Sc_2Si_3O_{12}:Cr^{3+}$ ($\lambda_{em,max}=770$ nm) exhibit an IQE approaching 100% and retain over 90% of the roomtemperature emission intensity at 423 K $(I_{423 \text{ K}})$, the accepted operating temperature of InGaN LEDs. 23,2

The high performance of the garnet family can be mainly ascribed to the high rigidity of the host structure and wide band gap of the host that can effectively suppress the photoionization process. Nevertheless, the densely packed atomic structure can give rise to a strong crystal field, causing the majority of Cr^{3+} -activated garnet materials to exhibit an emission peak wavelength below 800 nm. 100 nm. 100 This portion of the far-red region (650–780 nm) is not conducive to applications requiring NIR light. Consequently, there is a desire to shift the emission produced by garnet phosphors to a longer emission wavelength, ideally, $\lambda_{\rm em,max} \geq 800$ nm.

Designing a phosphor with electronic transitions in this region can be done by modulating the crystal field strength, as portrayed by the Tanabe–Sugano diagram. A specific example is the La₃In₂Ga₃O₁₂:Cr³⁺ phosphor, where a weak crystal field environment was engineered by selecting large ions to occupy cationic sites, resulting in the desired emission peak at 830 nm. Regrettably, the excitation peak of this material ($\lambda_{\rm ex}\approx 480$ nm) and the overall shape of the excitation peak do not align with the blue-emitting LED. This compound also shows a relatively low internal quantum efficiency (IQE < 40%), hindering practical application.

There is a possible solution to these challenges. Recent studies have demonstrated that the introduction of Jahn–Teller distortion effectively enhances the generation of long-wavelength emission by increasing the splitting of the d energy levels. $^{32-34}$ Based on this effect, the successful design of $\rm Ca^{2+}$ $\rm Zr^{4+}/Hf^{4+}$ and $\rm Zn^{2+}-\rm Ga^{3+}$ mixed ions occupying octahedral sites in the base $\rm Gd_3Sc_2Ga_3O_{12}$ garnets has achieved emission peak wavelengths surpassing 830 nm while maintaining excitation with blue light. 32,35,36 Unfortunately, the heavy substitution killed the IQE of these heavily distorted garnets, primarily due to the emergence of defects resulting from substantial size mismatches in octahedral sites. 35 Defects,

including antisite defects, surface defects, and the formation of Cr⁴⁺, act as quenching centers for Cr³⁺ by trapping excited electrons, leading to a comparatively low efficiency.^{23,35,37,38}

In this work, we aim to combine the advantages of a weak crystal field effect and Jahn-Teller distortion to create a garnet phosphor with a general composition, $A_3B_2C_3O_{12}$, that can be excited by blue light and efficiently emit relatively longwavelength NIR light even at elevated temperatures. With these criteria in mind, we settled on a phosphor following these design parameters: low-valence-state Na+, having an ionic radius even larger than La³⁺, was selected to occupy the A site to further reduce the crystal field strength. This choice necessitates substituting the B and C sites with higher-valencestate ions to maintain a charge balance. Consequently, Zr4+ and Ge4+ were selected for the octahedral and tetrahedral sites, respectively. To minimize defects and stabilize the Cr³⁺ valence state, Na⁺/Ca²⁺ cooccupancy in the A site was finally implemented for charge self-balancing. This resulting composition, Na₂CaZr₂Ge₃O₁₂, was anticipated to have a weak crystal field and suitable distortion induced by Na+/Ca2+ with different ionic radii in the dodecahedral site, which proves beneficial for achieving long-wavelength NIR emission. Furthermore, the single-ion occupation in octahedral sites should minimize defects, promoting high efficiency. The synthesis of this targeted composition was ultimately achieved using a high-temperature solid-state reaction, while photoluminescence measurements demonstrated that, as anticipated, Na₂CaZr₂Ge₃O₁₂:Cr³⁺ exhibits a broadband NIR emission with a relatively long-wavelength peak at 832 nm. Notably, the IQE was measured at an impressive 98% for Na₂CaZr₂Ge₃O₁₂:0.02Cr³⁺, while increasing the Cr³⁺ led to a better external quantum efficiency (EQE) of 34% for Na₂CaZr₂Ge₃O₁₂:0.06Cr³⁺ (both under 455 nm blue light excitation). Moreover, the construction of a NIR pc-LED device, optimized for performance, surpasses those of previously reported phosphors with similar emission peaks. Finally, the potential of the fabricated device has also been estimated through multiple practical applications.

2. EXPERIMENTAL SECTION

2.1. Materials and Synthesis. Polycrystalline samples of $Na_2CaZr_{2-x}Ge_3O_{12}:xCr^{3+}$ (x = 0, 0.01, 0.02, 0.04, 0.06, 0.08, and 0.10) were prepared by a high-temperature solid-state reaction. The starting materials NaHCO3 (Aladdin, 99.95%), CaCO3 (Macklin, 99.99%), ZrO₂ (Aladdin, 99.99%), GeO₂ (Aladdin, 99.99%), and Cr₂O₃ (Aladdin, 99.99%) were used as received and weighed according to the stoichiometric ratio. To compensate for the evaporation of Na at elevated temperatures, an additional 5 mol % of NaHCO3 was added. The starting materials were thoroughly ground with an agate mortar and pestle for 30 min using ethanol as a wetting medium. The mixtures were subsequently placed into corundum crucibles as loose powder and sintered in a muffle furnace at 1624 K for 8 h in the air. The resulting products were ground into a fine powder by using an agate mortar and pestle. To enable direct comparison of the title phosphor with previously published materials, each displaying an emission peak maximum at 830 nm, these $compounds - Ga_{0.994} TaO_4: 0.006 Cr^{3+}, \ \ Li In_{0.94} Si_2O_6: 0.06 Cr^{3+}, \ \ and$ Ga_{1.57}Mg_{0.2}Ge_{0.2}O₃:0.03Cr³⁺—were also synthesized here following the original reports.³⁸⁻⁴⁰

2.2. Characterization. Powder X-ray diffractograms were collected for all prepared samples using an X'Pert³ PANalytical diffractometer (Cu K α , λ = 1.5406 Å). The products were confirmed to show near-phase purity, while unit cell parameters were obtained from refinements based on the Rietveld method using the General Structure Analysis System (GSAS) software and the EXPGUI

interface. 41,42 Visualization for Electronic and Structural Analysis (VESTA) was employed to visualize the crystal structure. 43 The morphology and chemical composition of the prepared samples were analyzed by a Hitachi S4800 (Japan) scanning electron microscope (SEM) and an X-ray energy-dispersive spectrometer (EDS), while an FEI Talos F200 electron microscope was employed to measure highresolution transmission electron microscopy (HRTEM) mapping. The diffuse reflectance (DR) spectrum was collected via an ultraviolet-visible-near-infrared (UV-vis-NIR) spectrophotometer (Shimadzu, Japan), and EPR (electron paramagnetic resonance) measurements were performed using an EPR spectrometer (Japan, JES-FA300) at liquid nitrogen temperature (77 K). X-ray photoelectron spectroscopy (XPS) measurements were carried out on a photoelectron spectrometer (K-Alpha, Thermo Scientific). An FLS-1000 fluorescence spectrophotometer (Edinburgh Instruments Ltd.) was utilized to record the photoluminescence excitation and emission spectra at room-temperature and fluorescence decay curves. For photoluminescence excitation and emission measurements, a 450 W continuous xenon arc lamp was used as the excitation source, while the decay traces were collected by using a 450 W Xe pulse lamp. Measurements of the internal quantum efficiency (IQE) and absorption efficiency (AE) were conducted by using a Quantaurus-QY Plus C13534-11 (Hamamatsu Photonics), which was equipped with an integrating sphere using BaSO₄ as a reference.

The NIR pc-LED devices were fabricated by uniformly integrating a mixture of optimal phosphors and resin in a 1:1 ratio onto the InGaN blue chips ($\lambda_{\rm em}=455$ nm). Devices were created incorporating the title phosphor and the previously reported phosphors: ${\rm Ga_{0.994}TaO_4:0.006Cr^{3+}}$, ${\rm LiIn_{0.94}Si_2O_6:0.06Cr^{3+}}$, and ${\rm Ga_{1.57}Mg_{0.2}Ge_{0.2}O_3:0.03Cr^{3+}.^{38-40}}$ Electroluminescence (EL) spectra, NIR output power, and photoelectric conversion efficiency of all NIR pc-LED devices were recorded by a HAAS2000 photoelectric measuring system (350–1000 nm, EVERFINE, China).

2.3. Computation. The electronic structure of $Na_2CaZr_2Ge_3O_{12}$ was analyzed using the Vienna ab initio simulation package (VASP), which is based on density functional theory (DFT). The crystal structure was first optimized by treating by creating an ordered distribution of Na^+ and Ca^{2+} on the dodecahedral site according to the overall composition. The electronic and atomic convergence criteria were set to be 1×10^{-5} eV and 0.01 eV/Å, respectively. The cutoff energy was set to 500 eV for the basis set of the plane waves, and a single Γ point was used to sample the first Brillouin zone for this large unit cell. The PBE exchange—correlation functional was utilized in structure optimization, electronic structure, and elastic constant calculations. The Debye temperature is calculated based on the calculated elastic constants and the arithmetic relations outlined by the quasi-harmonic Debye model. $^{45-47}$

3. RESULTS AND DISCUSSION

3.1. Crystal Structure, Density of States, and Diffuse Reflectance Spectra of Na₂CaZrGe₃O₁₂. One-step solidstate synthesis of the pristine, unsubstituted Na₂CaZrGe₃O₁₂ was achieved at 1624 K producing a highly crystalline singlephase product, as confirmed by laboratory powder X-ray diffraction (Figure 1a). The results indicate that the target material is isostructural with a Y₃Al₅O₁₂ garnet-type cubic crystal structure (ICSD #23848). The crystal structure was refined using the prototypical garnet structure starting point for Rietveld refinement. The dodecahedral site bore a combination of Na+ and Ca2+ in a 2:1 statistical mixture; Zr4+ replaced Al3+ on the octahedral site, and Ge4+ replaced Al³⁺ on the tetrahedral site. The resulting model was then refined with the unit cell parameters and atomic positions as symmetry-constrained variables. The results showed excellent agreement between the collected data and the structural model. The refinement details and refined atomic position are summarized in Tables 1 and S1, respectively. Na⁺ and Ca²⁺ are

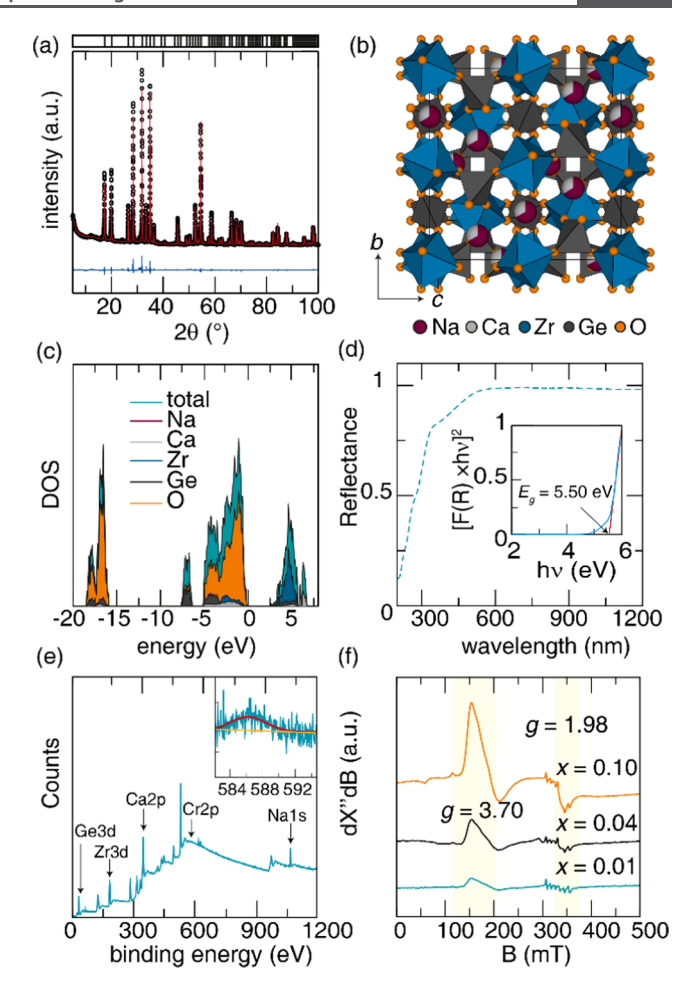


Figure 1. (a) Rietveld refinement of X-ray powder diffraction data for the Na₂CaZr₂Ge₃O₁₂ host. Black circles represent the measured data; the refinement is red, while the difference curve is blue. (b) Refined crystal structure of Na₂CaZr₂Ge₃O₁₂. (c) Density of states of Na₂CaZr₂Ge₃O₁₂ calculated by using a PBE functional. (d) Diffuse reflection spectrum of the unsubstituted Na₂CaZr₂Ge₃O₁₂ host material with the calculated optical band gap shown in the inset. (e) XPS spectra of the Na₂CaZr_{1.94}Ge₃O₁₂:0.06Cr³⁺ sample. (f) EPR spectra of Na₂CaZr_{2.x}Ge₃O₁₂:xCr³⁺ (x = 0.01, 0.04, and 0.10).

statistically mixed with a refined occupancy of 2:1 ratio, consistent with the nominally loaded composition.

The crystal structure of $Na_2CaZr_2Ge_3O_{12}$ belongs to the cubic crystal system in space group $Ia\overline{3}d$ (no. 230). The structure comprises mixed-occupancy Ca^{2+}/Na^+ ions located at Wyckoff position 12c. Each ion is dodecahedrally coordinated to eight oxygen atoms, which are shared with neighboring

Table 1. Rietveld Refinement Data of Na₂CaZr₂Ge₃O₁₂

formula	$Na_{2}CaZr_{2}Ge_{3}O_{12} \\$
radiation type; λ (Å)	X-ray; 1.5406
2θ (deg)	5-120
temperature (K)	298
space group	$Ia\overline{3}d$
$\alpha = \beta = \gamma \text{ (deg)}$	90.00
a = b = c (Å)	12.5916(7)
V (Å ³)	1996.40(1)
profile R-factor, R _p	0.0497
weighted profile R -factor, $R_{\rm wp}$	0.0779

[GeO₄] tetrahedra and [ZrO₆] octahedra, as depicted in Figure 1b. This arrangement forms a network of corner-connected octahedral [ZrO₆] and tetrahedral [GeO₄], resulting in a dense three-dimensional polyhedral network. To visualize the contribution of each element to the formation of a band gap in the examined compound, it is imperative to calculate the density of states. The DFT-PBE functional will underestimate the band gap, as presented in Figure 1c, but should be reliable for interpreting the basic electronic structure. The partial density of states indicates that the O 2p states dominate the top of the valence band, whereas the bottom of the conduction band consists of the Zr 4d states hybridized with the Ge 4s states. The electronic band gap revealed an (underestimated) indirect band gap value of 3.39 eV (Figure S1). To validate the determined indirect band gap, diffuse reflectance of the material was collected (Figure 1d). The absorption cutoff edge of the host is at ≈228 nm, and the Kubelka-Munk function^{38,48,49} is provided in eq 1

$$[h\nu\alpha]^{1/n} = A(h\nu - E_{\rm g}) \tag{1}$$

where hv represents the photon energy, α is the absorption coefficient, $E_{\rm g}$ is the value of the optical band gap, and A is a proportionality constant used to determine the band gap. The exponent n is dependent on the nature of the electronic transition and can be set to 1/2, 3/2, 2, and 3 for the direct allowed transition, direct forbidden transition, indirect allowed transition, and indirect forbidden transition, respectively.

The experimental optical band gap was found to be best described when n = 2, indicating the material has an indirect allowed transition, in agreement with the calculations. Based on this fitting, the experimental E_g was estimated to be 5.50 eV, surpassing many garnet hosts such as $Ca_3Sc_2Si_3O_{12}$ ($E_g = 4.21$ eV), $Y_3In_2Ga_3O_{12}$ ($E_g = 4.98$ eV), and $Na_3In_2Li_3F_{12}$ ($E_g = 5.30$ eV). 26,27,50 Such a wide band gap might indicate highphotoluminescence thermal stability when Cr3+ is incorporated in the material, as usually, a narrow band gap increases the likelihood of luminescence quenching via thermally activated photoionization. 51,52 However, beyond the band gap value, high structural rigidity within the host structure is frequently regarded as essential for designing efficient and thermally stable phosphor materials. The evaluation of structural rigidity can be achieved by determining the materials' Debye temperature (Θ_D) based on the DFT-PBE elastics constants. 53,54 The calculated Θ_D in $Na_2CaZr_2Ge_3O_{12}$ is found to be 486 K. This value aligns with other host structures that are known efficient NIR phosphors when substituted with Cr3+ such as $GaTaO_4$ ($\Theta_D = 567$ K, IQE = 91.2%), $LiInSi_2O_6$ ($\Theta_D =$ 550 K, IQE = 75%), and Ga_2O_3 (Θ_D = 530 K, IQE = 92.4%). These results indicate that the $Na_2CaZr_2Ge_3O_{12}$ host structure should be promising luminescent materials when activated with Cr³⁺ for NIR applications.

3.2. Cr^{3+} Substitution in $Na_2CaZr_{2-x}Ge_3O_{12}$. Incorporating Cr^{3+} and varying the concentration following $Na_2CaZr_{2-x}Ge_3O_{12}$: xCr^{3+} (x=0.01, 0.02, 0.04, 0.06, 0.08, and 0.10) produced a series of pure polycrystalline samples based on refinements of their powder X-ray diffractograms (Figure S2). As the concentration of Cr^{3+} increases, the lattice parameters and cell volume gradually decrease (Figure S3), indicating the likely substitution of the smaller Cr^{3+} (r_{6-coor} . = 0.62 Å) for the larger Zr^{4+} (r_{6-coor} . = 0.72 Å) on the octahedral sites. ⁵⁵

High-resolution transmission electron microscopy (HRTEM) for the Na₂CaZr_{1.94}Ge₃O₁₂:0.06Cr³⁺ sample was conducted to further confirm the structure, as presented in Figure S4a. The lattice fringes with a d-spacing of 0.261 nm were assigned to the (332) planes, which is slightly narrower than that (0.268 nm) in the undoped Na₂CaZr₂Ge₃O₁₂ simulated from the refined structural model. The morphology of Na₂CaZr_{1.94}Ge₃O₁₂:0.06Cr³⁺ was also examined by means of SEM, as shown in Figure S4b-i. The micrographs revealed that the particles have an irregular morphology with a size falling between 1 and 50 μ m. Mapping the elemental distribution using energy-dispersive X-ray spectrometry (EDS) indicated that the loaded elements are uniformly distributed in the region examined and no contamination was present from the synthesis (i.e., aluminum from the crucible). Furthermore, X-ray photoelectron spectroscopy (XPS) was utilized to determine the Cr valence state in the Na₂CaZr₂Ge₃O₁₂ host structure. As shown in Figure 1e, the resulting spectrum indeed supports the expected +3 valence state for Cr centered at 586.6 eV. 56,57

To further investigate the local structure and interactions around Cr^{3+} , electron paramagnetic resonance (EPR) spectra of $Na_2CaZr_{2-x}Ge_3O_{12}$: xCr^{3+} (x=0.01,0.04, and 0.10) samples were collected, as depicted in Figure 1f. In all analyzed samples, distinct signals appear at g=3.7 and 1.98, attributed to individual Cr^{3+} ions and coupled $Cr^{3+}-Cr^{3+}$ ion pairs within the octahedral site, respectively. With an increase in the concentration of Cr^{3+} in the host structures, the intensities at g=3.7 and 1.98 also increase. However, their dynamics reveal a notable contrast: the intensity at g=3.7 displays a more pronounced enhancement compared to that at g=1.98. This observation suggests that the majority of Cr^{3+} ions reside within the crystal in isolated states.

3.3. Photoluminescence Properties of the NIR Phosphor. Figure 2a presents the photoluminescence excitation and emission spectrum exhibits two intense absorption peaks in the blue and red regions of the visible spectrum corresponding to ${}^4A_2 \rightarrow {}^4T_1$ and ${}^4A_2 \rightarrow {}^4T_2$ Cr³⁺ intraconfigurational 3d \leftrightarrow 3d transitions, respectively. Monitoring the emission upon excitation at $\lambda_{\rm ex}=460$ nm leads to the intense broadband NIR luminescence with the maximum located at 832 nm and full width at half-maximum (fwhm) of 2054 cm⁻¹ (144 nm), indicating a typical emission of Cr³⁺ in a weak crystal field. The magnitude of crystal field splitting can be estimated by the crystal field strength (D_q) and Racah parameter (B) value using eqs $2-4^{3,60}$

$$10D_{q} = E(^{4}T_{2}) = E(^{4}A_{2} \to {}^{4}T_{2})$$
(2)

$$\frac{D_{\rm q}}{B} = \frac{15(x-8)}{x^2 - 10x} \tag{3}$$

$$x = \frac{E(^{4}A_{2} \to {}^{4}T_{1}) - E(^{4}A_{2} \to {}^{4}T_{1})}{D_{q}}$$
(4)

The value of the Dq/B ratio is found to be 1.99. According to the Tanabe–Sugano diagram, this confirms that Cr³⁺ is situated in a weak crystal field environment as desired (Figure S5).

Examining the emission spectra of $Na_2CaZr_{2-x}Ge_3O_{12}$: xCr^{3+} (x = 0.01, 0.02, 0.04, 0.06, 0.08, and 0.10), plotted in Figure 2b and excitation spectra (Figure S6), offers further insight into

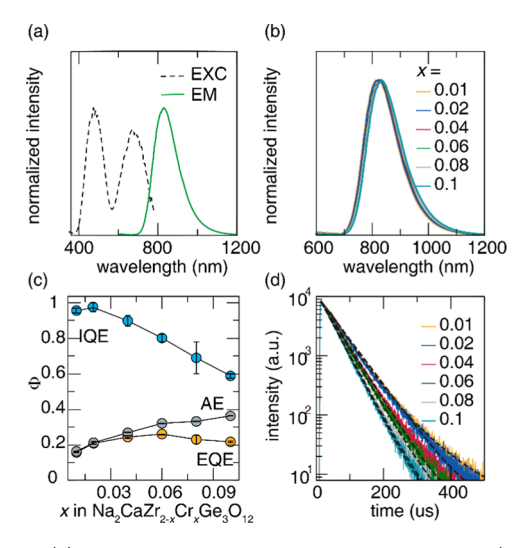


Figure 2. (a) Normalized photoluminescence excitation (exc) and emission (em) spectra of the Na₂CaZr_{1.94}Ge₃O₁₂:0.06Cr³⁺ sample. (b) Normalized photoluminescence spectra of Na₂CaZr_{2-x}Ge₃O₁₂:xCr³⁺ (x=0.01, 0.02, 0.04, 0.06, 0.08, and 0.10). (c) Room-temperature internal quantum efficiency (IQE), absorption efficiency (AE), and external quantum efficiency (EQE) measurements of Na₂CaZr_{2-x}Ge₃O₁₂:xCr³⁺ (x=0.01, 0.02, 0.04, 0.06, 0.08, and 0.10) under 460 excitation. (d) Room-temperature decay curves of Na₂CaZr_{2-x}Ge₃O₁₂:xCr³⁺ (x=0.01, 0.02, 0.04, 0.06, 0.08, and 0.10).

the luminescent characteristics of this phosphor. Despite varying the Cr³+ concentration, there is no noticeable shift in the excitation peaks. The consistent position of the excitation spectrum suggests that the crystal field splitting remains largely unaffected by variations in the concentration of Cr³+. This stability primarily arises from the rigid nature of the crystal structure and the low substitution concentration, which do not disturb the overall crystal structure. Conversely, a slight red shift can be seen when analyzing the emission spectra, which is likely due to spectral overlap between excitation and emission peaks, leading to the reabsorption process.

The room-temperature IQE, absorption efficiency (AE), and external photoluminescence quantum efficiency (EQE) were measured under λ_{ex} = 460 nm. As observed in Figure 2c, the IQE initially has an impressive efficiency of 98.4% when x =0.02; however, it immediately decreases at higher concentrations due to concentration quenching caused by energy migration between neighboring Cr3+ centers, and the increased possibility of forming defects caused by the aliovalent Cr³⁺ substitution for Zr⁴⁺. Nevertheless, the maximum value of IQE is higher than those of most NIR materials when the emission peak is centered above 800 nm. This includes Lu- $Ca_2ScZrGa_2GeO_{12}:Cr^{3+}$ ($\lambda_{em}=815$ nm, IQE=68.8%), $La_2MgZrO_6:Cr^{3+}$ ($\lambda_{em}=825$ nm, IQE=58%), and $LiScSi_2O_6:Cr^{3+}$ ($\lambda_{em}=845$ nm, IQE=64.4%). The AE and EQE values also increase with increasing Cr3+ concentration. This can be attributed to the improved absorption of the incident excitation energy by the phosphor. Similar to most garnet materials, the AE value is not the highest among Cr³⁺activated materials mainly due to the high structure symmetry of garnet, which is unfavorable to breaking the parity-forbidden transitions.⁶⁴ However, the combined exceptional IQE and the moderate EQE (maximally 34%) of this phosphor directly from the furnace suggest there is potential for further

improvement through additional optimization and postsynthesis processing.

Room-temperature photoluminescence decay curves of $Na_2CaZr_{2-x}Ge_3O_{12}$: xCr^{3+} ($x=0.01,\ 0.02,\ 0.04,\ 0.06,\ 0.08,$ and 0.10) are presented in Figure 2d upon excitation with 460 nm light. All of the decay curves are described by a single-exponential function as presented in eq $5^{61,63}$

$$I_t = I_0 + A \exp\left(-\frac{t}{\tau}\right) \tag{5}$$

where I_0 stands for the offset, I_t represents intensity at time t, A represents the fitting constant, and τ is the lifetime. The obtained lifetime gradually decreases from 54.8 to 40.2 μ s with increasing Cr^{3+} concentration, stemming from the gradually enhanced interactions between Cr^{3+} ions, which lead to energy loss in nonradiative transitions.

3.4. Thermal Stability of NIR Emission. To delve deeper into the luminescence properties of the investigated material and assess its potential in real-life applications, the sample containing 6% $\rm Cr^{3+}$ (highest EQE) was studied in detail. Collecting the temperature-dependent emission spectra of the Na₂CaZr_{1.94}Ge₃O₁₂:0.06Cr³⁺ sample in the 298–473 K temperature range reveals that the emission intensity gradually decreases as the temperature increases. Figure 3a,b presents

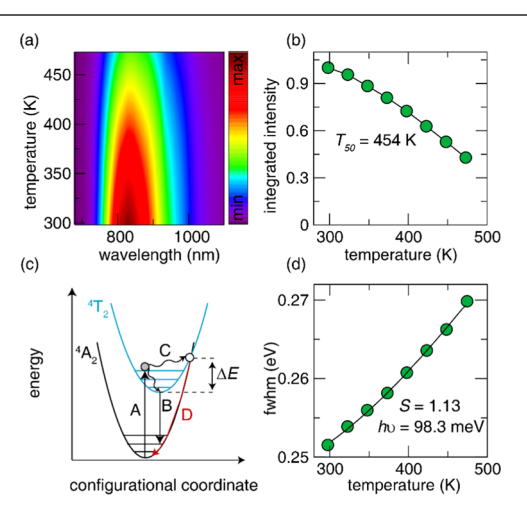


Figure 3. (a) Contour plot of the temperature-dependent PL spectra of $Na_2CaZr_{1.94}Ge_3O_{12}:0.06Cr^{3+}$. (b) Normalized integrated intensity of $Na_2CaZr_{1.94}Ge_3O_{12}:0.06Cr^{3+}$ as a function of temperature. (c) Configuration coordination mechanism responsible for thermal quenching, (d) Fitted Huang–Rhys factor *S*.

the contour plot of spectra together with integrated intensity as a function of temperature, while the raw spectra are provided in Figure S7. The material retains 62.8% of the room-temperature intensity at 423 K. These results demonstrate reasonably high thermal stability compared with materials with similar emission peak wavelengths, such as $GaTaO_4:Cr^{3+}$ ($I_{423~K}=60\%$), $BaZrGe_3O_9:Cr^{3+}$ ($I_{423~K}=53\%$), and $Ga_{1.6}Mg_{0.2}Ge_{0.2}O_3:Cr^{3+}$ ($I_{423~K}=42.8\%$).

The thermal stability of phosphors typically hinges on two primary mechanisms: thermally activated photoionization and crossover process. Considering the wide band gap of the $Na_2CaZr_2Ge_3O_{12}$ host structure ($E_g=5.50$ eV), it is unlikely to induce thermal quenching via photo- or thermal-ionization processes. The thermal quenching of the phosphor is therefore likely to occur through a mechanism involving a

thermally activated crossover process. This process takes place when the potential energy surfaces of the ground and excited states intersect, as illustrated in Figure 3c. The absorption of radiation quanta results in the excitation of an electron situated at the lowest electronic and vibrational levels, propelling it to the edge of the excited parabola (process A). Following, the electron undergoes a nonradiative relaxation process, descending to the lowest vibrational level of the excited state and releasing excess energy into the surroundings as heat. Consequently, the electron may spontaneously relax to the ground state, emitting a photon of light in the process. When a substantial offset exists between the potential energy surfaces of the excited state and ground state, the possibility of their intersection (process C) arises. This intersection facilitates the nonradiative relaxation of the excited state, typically resulting in the release of energy in the form of heat (process D). Therefore, it is imperative to determine the parabola offset in the Na₂CaZr_{1.94}Ge₃O₁₂:0.06Cr³⁺ material, which is controlled by the magnitude of the electron-phonon coupling and can be characterized by the Huang-Rhys factor (S). The value of S can be calculated by eq 65,

fwhm
$$(T) = \sqrt{8 \ln 2} \times \sqrt{S} \times hv \times \sqrt{\coth\left(\frac{hv}{2kT}\right)}$$
 (6)

where fwhm (T) is the full width at half-maximum of emission spectra at temperature T, $h\nu$ is the phonon energy, and k stands for Boltzmann's constant (8.617 \times 10⁻⁵ eV/K).

As shown in Figure 3d, the calculated S and hv values for the title phosphor were determined to reach 1.13 and 98.3 meV, respectively. These values are close to the values estimated by the empirical equation $S = (1/2EStokes/hv + 1/4) \pm 1/4$ (Figure S8). Compared to other reported NIR phosphors, such as $La_3Sc_2Ga_3O_{12}$: Cr^{3+} (S = 6.0), ScF_3 : Cr^{3+} (S = 3.01), and K_2 NaScF₆:Cr³⁺ (S = 2.96), this value is notably low indicating a weak electron-phonon coupling effect in the title material. 31,68,69 This finding aligns with the determined $\Theta_{\rm D}$ temperature for this composition (486 K). However, considering the temperature-dependent luminescence data, this is somehow surprising as weak electron-phonon coupling typically signifies high thermal stability. Here, a decrease in luminescence intensity, albeit small, is observed above 300 K. This discrepancy might be attributed to the fact that structural distortion within the host can notably diminish the S value, as discussed previously.³⁵ Therefore, the obtained S value might not entirely represent the EPC effect in materials with dodecahedral site distortion.

The alternative mechanism of photoionization could also be related to the anomalous thermal quenching behavior. Although initially discounted based on the wide $E_{\rm g}$ of the phosphor host, it is still a possible quenching pathway based on the position of the ${\rm Cr}^{3+}$ 3d orbitals and the host conduction band. To further investigate the nature of this thermal quenching pathway, an activation energy (ΔE) was calculated, which acts as the energy barrier for excited electrons to pass the intersection, causing nonradiative transitions, and can be estimated following eq $7^{3,9,62,63}$

$$I_{\rm T} = \frac{I_0}{1 + C \exp\left(-\frac{\Delta E}{kT}\right)} \tag{7}$$

where I_0 represents the emission intensity at 298 K, I_T is the intensity at temperature T, and C is a constant. As presented in

Figure S9, the ΔE from this analysis can be determined to be 0.284 eV, which is lower than LiScP₂O₇:Cr³⁺ (ΔE = 0.337 eV), ScBO₃:Cr³⁺ (ΔE = 0.36 eV), and GdAl₃(BO₃)₄:Cr³⁺ (ΔE = 0.41 eV). This is a relatively low thermal barrier, indicating, indeed, a high probability of thermal quenching at elevated temperatures. Consequently, improving this material necessitates exploring techniques for chemically altering the phosphor, which elevates the activation barrier to prevent the crossover process.

3.5. NIR Pc-LED Fabrication and Applications. To evaluate the potential of the phosphor in a pc-NIR LED application, several parameters should be considered, such as fwhm, thermal stability, efficiency, and spectral coverage. Figure 4a presents a comparison of some promising garnet-

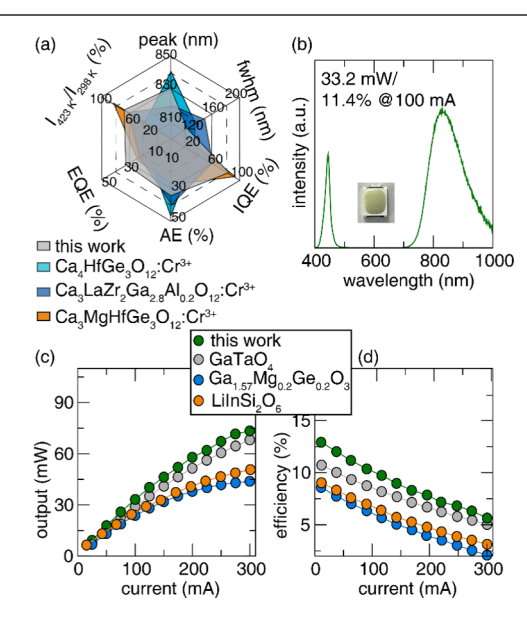


Figure 4. (a) Comparison of properties with some relatively long-wavelength-emitting garnet materials. (b) EL spectra of Na₂CaZr_{1,94}Ge₃O₁₂:0.06Cr³⁺-containing pc-LED devices under 100 mA driving current and the photograph of the device. A comparison of (c) NIR output power and (d) electric-photoconversion efficiency of the fabricated NIR pc-LED devices within a driving current of 25–300 mA.

type materials along with the material investigated in the given work.^{29,35,73} Among all of the presented compounds, Na₂CaZr₂Ge₃O₁₂:Cr³⁺ stands out for its noteworthy attributes: longer-wavelength emission, the highest observed IQE and EQE, and a commendable level of thermal stability. These characteristics distinguish it prominently within the category of garnet NIR phosphors. This unique combination of properties positions it as a promising candidate worthy of testing to verify the potential application. Thus, a prototype NIR pc-LED device was fabricated by coating a blue LED chip ($\lambda_{em} = 455$ nm) with the Na₂CaZr_{1.94}Ge₃O₁₂:0.06Cr³⁺ phosphor encapsulated in a silicone resin. The electroluminescence (EL) spectra driven by 100 mA current were collected and are plotted in Figure 4b, accompanied by an inset featuring a photograph of the device. The measured NIR output power was found to be 33.2 mW, giving rise to a NIR photoelectric conversion efficiency of 11.4% (at 100 mA). This combination of LED and phosphor outperforms all other devices utilizing garnet materials (as listed in Table S2).

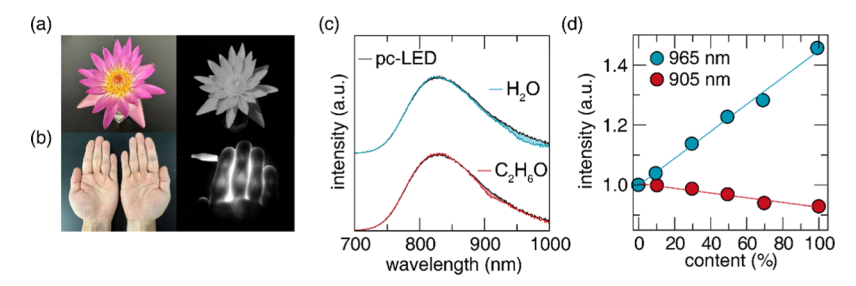


Figure 5. (a) Lotus and (b) fingers digital photography captured under daylight light and NIR camera. (c) Transmission spectra of H_2O and C_2H_6O comparing with emission spectra of the pc-LED device. (d) Linear relationship between absorption at 905 and 965 nm of alcohol solutions with different concentrations.

The superior performance of Na₂CaZr_{1.94}Ge₃O₁₂:0.06Cr³⁺ in this device was, therefore, demonstrated by direct comparison with several other efficient NIR phosphors, all known for their peak wavelengths of more than 830 nm. The samples were all resynthesized here, and the corresponding X-ray diffractogram patterns are provided in Figure S10. These phosphors were also fabricated into NIR pc-LEDs and measured under identical conditions. As plotted in Figure 4c, the NIR output shows an incremental increase with increasing driving currents for all devices. However, within the 25-300 mA range tested here, the device utilizing the Na₂CaZr_{1.94}Ge₃O₁₂:0.06Cr³⁺ phosphor consistently exhibits the highest output power. At the same time, Figure 4d provides each device's NIR photoelectric conversion efficiency. Driving the phosphor shows an overall gradual decrease as a function of the driving current throughout the range. This reduction is primarily attributed to the "efficiency droop" phenomenon of the blue InGaN LED chip. 29,35,38 Nevertheless, because a same millimeter LED was used for each device, these results demonstrate that incorporating the Na₂CaZr_{1.94}Ge₃O₁₂:0.06Cr³⁺ phosphor produces a NIR pc-LED that outperforms the others, showing the smallest drop as a function of driving current. Indeed, a better NIR photoelectric conversion efficiency is obtained for all driving currents up to 300 mA. Hence, a comprehensive analysis of both NIR output power and photoelectric conversion efficiency consistently establishes that the Na₂CaZr_{1.94}Ge₃O₁₂:0.06Cr³⁺ phosphor stands out as the superior choice among all investigated materials. Its performance surpasses that of the other tested phosphors across varying driving currents, emphasizing its excellence for applications in NIR-emitting devices.

The real-world potential of the Na₂CaZr_{1.94}Ge₃O₁₂:0.06Cr³⁺ material was finally assessed through various experiments including night vision, imaging, and analytical chemical analysis. In Figure 5a, a digital image of a flower captured under daylight conditions is compared with a nighttime photograph taken by using a NIR camera. Notably, the blackand-white image illuminated by NIR light distinctly reveals the intricate details of the flower, highlighting the utility of this technology as the light source for night-vision applications. Similarly, Figure 5b illustrates a comparison between photographs of a hand taken in natural light and those taken in NIR light. Under the NIR light, the blood vessels in the fingers are evident, suggesting the potential application of this device in biomedical imaging or nondestructive examinations. Finally, the fabricated NIR pc-LED device was used as the excitation source to measure the transmission spectra for various alcohol concentrations. These data were collected by inserting a

cuvette with alcohol solutions into the sample chamber's optical path. Collecting the absorption spectra clearly reveals characteristic absorption bands at 970 and 910 nm, which can be assigned to the second overtones of the O–H stretching band and to the third frequency of the C–H bond, respectively (Figure 5c). Based on this, the absorption of alcohol solutions at various concentrations was measured and is depicted in Figure S11. The linear fit of the relationship between absorbance intensity and alcohol concentration (plotted in Figure 5d) at 965 and 905 nm, with goodness of fit values $R^2 = 0.990$ and 0.993, respectively, suggests an excellent potential for utilizing this material in nondestructive and quantitative analysis using the vibrational spectra. 32,74

4. CONCLUSIONS

In summary, a new garnet-type phosphor, Na2CaZr2Ge3O12:Cr3+, was developed using the crystalchemical understanding of Cr3+ developed over the past few years. The targeted composition was successfully synthesized through a high-temperature solid-state reaction, and the optimized sample containing a Cr^{3+} concentration of x =0.06 was shown to exhibit a broad near-infrared (NIR) emission spanning from 700 to 1150 nm, with a peak at 832 nm when excited at 455 nm. Remarkably, Na₂CaZr_{1.98}Ge₃O₁₂:0.02Cr³⁺ achieves a high internal quantum efficiency (IQE) of 98%, and Na₂CaZr_{1.94}Ge₃O₁₂:0.06Cr³⁺ possesses a high external quantum efficiency (EQE) of 34%. The properties could likely be further improved through synthesis optimization, including charge compensation and/or using flux to mitigate defect formation. The emission intensity also retains 62.8% of its room-temperature value, indicating a serviceable thermal stability. The manufactured NIR phosphorconverted light-emitting diode (pc-LED) device demonstrates outstanding performance with an output power of 33.2 mW and a photoelectric conversion efficiency of 11.4% under a 100 mA driving current. These results showcase significant advantages of Na₂CaZr₂Ge₃O₁₂:Cr³⁺ over previously reported phosphors with similar emission wavelengths. Additionally, the device exhibits multifarious applications such as night vision or detection of ethanol concentration in solution, underscoring the substantial potential of this material for NIR applications.

ASSOCIATED CONTENT

Supporting Information

The Supporting Information is available free of charge at https://pubs.acs.org/doi/10.1021/acs.chemmater.4c00426.

Electronic band structure, XRD patterns, HRTEM, SEM and elemental mapping images, Tanabe—Sugano diagram, PLE spectra, temperature-dependent PL spectra,

activation energy, transmission spectra, refined atomic positions, and NIR output performance (PDF)

AUTHOR INFORMATION

Corresponding Authors

Jiyou Zhong — School of Physics and Optoelectronic Engineering, Guangdong University of Technology, Guangzhou 510006, China; orcid.org/0000-0003-2817-6617; Email: zhongjiyou@126.com

Jakoah Brgoch — Department of Chemistry, University of Houston, Houston, Texas 77204, United States; orcid.org/0000-0002-1406-1352; Email: jbrgoch@uh.edu

Authors

Zurong Liao – School of Physics and Optoelectronic Engineering, Guangdong University of Technology, Guangzhou 510006, China

Małgorzata Sójka – Department of Chemistry, University of Houston, Houston, Texas 77204, United States;
orcid.org/0000-0001-9346-8929

Complete contact information is available at: https://pubs.acs.org/10.1021/acs.chemmater.4c00426

Author Contributions

§Z.L. and M.S. contributed equally to this paper.

Notes

The authors declare no competing financial interest.

ACKNOWLEDGMENTS

M.S. and J.B. thank the National Science Foundation (DMR-1847701) in the United States of America for supporting this work. Z.L. and J.Z. thank the National Natural Science Foundation of China (52372139), the Guangzhou Basic and Applied Basic Research Project (202201010689), and the Analysis and Test Center of Guangdong University of Technology for also providing research support.

REFERENCES

- (1) Szymczak, M.; Runowski, M.; Lavín, V.; Marciniak, L. Highly Pressure-Sensitive, Temperature Independent Luminescence Ratiometric Manometer Based on MgO:Cr³⁺ Nanoparticles. *Laser Photonics Rev.* **2023**, *17* (4), No. 2200801, DOI: 10.1002/lpor.202200801.
- (2) Zhang, J.; Mu, W.; Zhang, K.; Sun, J.; Zhang, J.; Lin, N.; Zhao, X.; Jia, Z.; Tao, X. Broadband Near-Infrared Cr^{3+} : β -Ga₂O₃ Fluorescent Single Crystal Grown by the EFG Method. *CrystEng-Comm* **2020**, 22 (44), 7654–7659.
- (3) Zhang, Y.; Miao, S.; Liang, Y.; Liang, C.; Chen, D.; Shan, X.; Sun, K.; Wang, X.-J. Blue LED-Pumped Intense Short-Wave Infrared Luminescence Based on Cr³⁺-Yb³⁺-Co-Doped Phosphors. *Light: Sci. Appl.* **2022**, *11* (1), No. 136, DOI: 10.1038/s41377-022-00816-6.
- (4) Rajendran, V.; Chen, K.-C.; Huang, W.-T.; Kamiński, M.; Grzegorczyk, M.; Mahlik, S.; Leniec, G.; Lu, K.-M.; Wei, D.-H.; Chang, H.; Liu, R.-S. Unraveling Luminescent Energy Transfer Pathways: Futuristic Approach of Miniature Shortwave Infrared Light-Emitting Diode Design. ACS Energy Lett. 2023, 8 (5), 2395–2400.
- (5) He, S.; Zhang, L.; Wu, H.; Wu, H.; Pan, G.; Hao, Z.; Zhang, X.; Zhang, L.; Zhang, H.; Zhang, J. Efficient Super Broadband NIR Ca₂LuZr₂Al₃O₁₂:Cr³⁺,Yb³⁺ Garnet Phosphor for Pc-LED Light Source toward NIR Spectroscopy Applications. *Adv. Opt. Mater.* **2020**, 8 (6), No. 1901684.

- (6) De Guzman, G. N. A.; Rajendran, V.; Bao, Z.; Fang, M.-H.; Pang, W.-K.; Mahlik, S.; Lesniewski, T.; Grinberg, M.; Molokeev, M. S.; Leniec, G.; Kaczmarek, S. M.; Ueda, J.; Lu, K.-M.; Hu, S.-F.; Chang, H.; Liu, R.-S. Multi-Site Cation Control of Ultra-Broadband Near-Infrared Phosphors for Application in Light-Emitting Diodes. *Inorg. Chem.* **2020**, *59* (20), 15101–15110.
- (7) Liu, G.; Hu, T.; Molokeev, M. S.; Xia, Z. Li/Na Substitution and Yb³⁺ Co-Doping Enabling Tunable near-Infrared Emission in LiIn₂SbO₆:Cr³⁺ Phosphors for Light-Emitting Diodes. *iScience* **2021**, 24 (4), No. 102250.
- (8) Huang, D.; Liang, S.; Chen, D.; Hu, J.; Xu, K.; Zhu, H. An Efficient Garnet-Structured Na₃Al₂Li₃F₁₂:Cr³⁺ Phosphor with Excellent Photoluminescence Thermal Stability for Near-Infrared LEDs. *Chem. Eng. J.* **2021**, *426*, No. 131332.
- (9) Cai, H.; Liu, S.; Song, Z.; Liu, Q. Tuning Luminescence from NIR-I to NIR-II in Cr³⁺ -Doped Olivine Phosphors for Non-destructive Analysis. *J. Mater. Chem. C* **2021**, *9* (16), 5469–5477.
- (10) Zuo, J.; Nie, W.; Li, Y.; Xie, H.; Gao, J.; Lai, W.; Li, X.; Peng, J.; Ye, X. Zero Thermal Quenching and Suppressed Concentration Quenching in a Highly Efficient Structure-confined Fluoride Near-Infrared Phosphor. J. Alloys Compd. 2023, 968, No. 171957.
- (11) Jin, C.; Li, R.; Liu, Y.; Zhang, L.; Zhang, J.; Sun, P.; Luo, Z.; Jiang, J. Efficient and Stable $Gd_3Ga_5O_{12}$: Cr^{3+} Phosphors for High-Performance NIR LEDs. *Adv. Opt. Mater.* **2023**, *11* (21), No. 2300772.
- (12) Wang, J.; Han, X.; Zhou, Y.; Wu, Z.; Liu, D.; Zeng, C.; Cao, S.; Zou, B. Ion Substitution Strategy toward High-Efficiency Near-Infrared Photoluminescence of $Cs_2KIn_{1-y}Al_yF_6$: Cr^{3+} Solid Solutions. *J. Phys. Chem. Lett.* **2023**, *14* (6), 1371–1378.
- (13) Yang, S.; Wang, Y.; Xiang, G.; Jiang, S.; Li, L.; Ling, F.; Hu, H.; Zhang, Y.; Zhou, X.; Suchocki, A. Luminescence Properties and Phase Transformation of Broadband NIR Emitting $A_2(WO_4)_3$: Cr^{3+} (A = Al^{3+} , Sc^{3+}) Phosphors toward NIR Spectroscopy Applications. *J. Lumin.* **2023**, 253, No. 119445.
- (14) Wang, C.; Jin, Y.; Yuan, L.; Wang, B.; Zhang, R.; Wu, H.; Yao, Q.; Hu, Y. Highly Efficient and Thermally Stable Broadband NIR Phosphors by Rationally Bridging Cr³⁺ Yb³⁺ in LiScGe₂O₆ for Optical Bioimaging. *Inorg. Chem. Front.* **2023**, *10* (3), 860–868.
- (15) Chen, L.; Wu, Y.; Liu, Q.; Guo, Y.; Liu, F.; Wang, B.; Wei, S. Energy Conversion and Transfer in the Luminescence of CeSc₃(BO₃)₄:Cr³⁺ Phosphor. *Materials* **2023**, *16* (3), No. 1231, DOI: 10.3390/ma16031231.
- (16) Zhang, L.; Wang, D.; Liu, F.; Wu, H.; Pan, G.; Wu, H.; Hao, Z.; Zhang, H.; Zhang, J. Minimizing Bond Angle Distortion to Improve Thermal Stability of Cr³⁺ Doped Near-Infrared Phosphor. *Laser Photonics Rev.* **2023**, *17* (9), No. 2300092.
- (17) Wang, T.; Wang, Y.; Chen, W.; Xia, Z. Crystallization of Na₂SrGe₆O₁₄:Cr³⁺,Yb³⁺ Glass Ceramics Enabling a Watt-Level Output Power NIR-I/NIR-II Lighting Source. *Laser Photonics Rev.* **2024**, *18* (1), No. 2300784.
- (18) Zhang, Q.; Wei, X.; Zhou, J.; Milićević, B.; Lin, L.; Huo, J.; Li, J.; Ni, H.; Xia, Z. Thermal Stability Improvement of Cr³⁺ -Activated Broadband Near-Infrared Phosphors via State Population Optimization. *Adv. Opt. Mater.* **2023**, *11* (14), No. 2300310.
- (19) Zhang, J.; Zhang, L.; Liu, F.; Wu, H.; Wu, H.; Pan, G.; Luo, Y.; Hao, Z.; Zhang, J. Smaller Stokes Shift Induced Highly Efficient Broadband Near Infrared Garnet Phosphor. *Laser Photonics Rev.* **2023**, 17 (2), No. 2200586.
- (20) Liu, G.; Molokeev, M. S.; Lei, B.; Xia, Z. Two-Site Cr^{3+} Occupation in the $MgTa_2O_6$: Cr^{3+} Phosphor toward Broad-Band near-Infrared Emission for Vessel Visualization. *J. Mater. Chem. C* **2020**, 8 (27), 9322–9328.
- (21) Zhou, X.; Xiang, J.; Zheng, J.; Zhao, X.; Suo, H.; Guo, C. *Ab Initio* Two-Sites Occupancy and Broadband Near-Infrared Emission of Cr³⁺ in Li₂MgZrO₄. *Mater. Chem. Front.* **2021**, *5* (11), 4334–4342. (22) Wu, H.; Jiang, L.; Li, K.; Li, C.; Zhang, H. Design of Broadband Near-Infrared Y_{0.57}La_{0.72}Sc_{2.71}(BO₃)₄:Cr³⁺ Phosphors Based on One-Site Occupation and Their Application in NIR Light-Emitting Diodes. *J. Mater. Chem. C* **2021**, *9* (35), 11761–11771.

- (23) Basore, E. T.; Wu, H.; Xiao, W.; Zheng, G.; Liu, X.; Qiu, J. High-Power Broadband NIR LEDs Enabled by Highly Efficient Blueto-NIR Conversion. *Adv. Opt. Mater.* **2021**, *9* (7), No. 2001660.
- (24) Jia, Z.; Yuan, C.; Liu, Y.; Wang, X.-J.; Sun, P.; Wang, L.; Jiang, H.; Jiang, J. Strategies to Approach High Performance in Cr³⁺-Doped Phosphors for High-Power NIR-LED Light Sources. *Light: Sci. Appl.* **2020**, 9 (1), No. 86, DOI: 10.1038/s41377-020-0326-8.
- (25) Jiang, L.; Jiang, X.; Zhang, L.; Liu, Q.; Mi, X.; Yu, Z.; Lv, G.; Su, Y. Broadband Near-Infrared Luminescence in Garnet Y₃Ga₃MgSiO₁₂:Cr³⁺ Phosphors. *Inorg. Chem.* **2023**, *62* (10), 4220–4226.
- (26) Li, C.; Zhong, J. Highly Efficient Broadband Near-Infrared Luminescence with Zero-Thermal-Quenching in Garnet Y₃In₂Ga₃O₁₂:Cr³⁺ Phosphors. *Chem. Mater.* **2022**, 34 (18), 8418–8426.
- (27) Zhou, Y.; Li, X.; Seto, T.; Wang, Y. A High Efficiency Trivalent Chromium-Doped Near-Infrared-Emitting Phosphor and Its NIR Spectroscopy Application. ACS Sustainable Chem. Eng. 2021, 9 (8), 3145–3156.
- (28) Dang, P.; Wei, Y.; Liu, D.; Li, G.; Lin, J. Recent Advances in Chromium-Doped Near-Infrared Luminescent Materials: Fundamentals, Optimization Strategies, and Applications. *Adv. Opt. Mater.* **2023**, *11* (3), No. 2201739.
- (29) Li, C.; Zhong, J. Efficient and Thermally Robust Broadband Near-Infrared Emission in a Garnet Ca₃MgHfGe₃O₁₂:Cr³⁺ Phosphor. *Adv. Opt. Mater.* **2023**, *11* (3), No. 2202323.
- (30) Zhao, F.; Song, Z.; Liu, Q. Advances in Chromium-Activated Phosphors for Near-Infrared Light Sources. *Laser Photonics Rev.* **2022**, 16 (11), No. 2200380.
- (31) Malysa, B.; Meijerink, A.; Jüstel, T. Temperature Dependent Cr^{3+} Photoluminescence in Garnets of the Type $X_3Sc_2Ga_3O_{12}$ (X = Lu, Y, Gd, La). *J. Lumin.* **2018**, 202, 523–531.
- (32) Wang, Y.; Wang, Z.; Wei, G.; Yang, Y.; He, S.; Li, J.; Shi, Y.; Li, R.; Zhang, J.; Li, P. Ultra-Broadband and High Efficiency Near-Infrared Gd₃Zn_xGa_{5-2x}Ge_xOl₂:Cr³⁺ (x = 0-2.0) Garnet Phosphors via Crystal Field Engineering. *Chem. Eng. J.* **2022**, 437, No. 135346.
- (33) Zeng, L.; Zhong, J.; Liu, H.; Zhao, W. Introducing Jahn-Teller Distortion to Enhance the Practicability of (Ga,Sc)₂O₃:Cr³⁺ near-Infrared Phosphor. *J. Lumin.* **2023**, 258, No. 119816.
- (34) Zeng, L.; Zhong, J.; Lin, W.; Zhao, W. Achieving a Tunable and Ultra-Broadband Near-Infrared Emission in the Ga_{2-2x}Zn_xGe_xO₃:Cr³⁺ Phosphor. *Dalton Trans.* **2022**, *51* (43), 16740–16747.
- (35) Liao, Z.; Zhong, J.; Li, C.; Jiang, H.; Zhao, W. Understanding the Broadband Near-Infrared Luminescence in a Highly Distorted Garnet $Ca_4HfGe_3O_{12}:Cr^{3+}$ Phosphor. *Phys. Chem. Chem. Phys.* **2023**, 25 (22), 15452–15462.
- (36) Xiang, J.; Zheng, J.; Zhao, X.; Zhou, X.; Chen, C.; Jin, M.; Guo, C. Synthesis of Broadband NIR Garnet Phosphor Ca₄ZrGe₃O₁₂:Cr³⁺, Yb³⁺ for NIR Pc-LED Applications. *Mater. Chem. Front.* **2022**, *6* (4), 440–449.
- (37) Jiang, H.; Chen, L.; Zheng, G.; Luo, Z.; Wu, X.; Liu, Z.; Li, R.; Liu, Y.; Sun, P.; Jiang, J. Ultra-Efficient GAGG:Cr³⁺ Ceramic Phosphor-Converted Laser Diode: A Promising High-Power Compact Near-Infrared Light Source Enabling Clear Imaging. *Adv. Opt. Mater.* **2022**, *10* (11), No. 2102741.
- (38) Zhong, J.; Zhuo, Y.; Du, F.; Zhang, H.; Zhao, W.; You, S.; Brgoch, J. Efficient Broadband Near-Infrared Emission in the GaTaO₄:Cr³⁺ Phosphor. *Adv. Opt. Mater.* **2022**, *10* (2), No. 2101800.
- (39) Xu, X.; Shao, Q.; Yao, L.; Dong, Y.; Jiang, J. Highly Efficient and Thermally Stable Cr³⁺-Activated Silicate Phosphors for Broadband Near-Infrared LED Applications. *Chem. Eng. J.* **2020**, 383, No. 123108.
- (40) Zhong, J.; Zeng, L.; Zhao, W.; Brgoch, J. Producing Tunable Broadband Near-Infrared Emission through Co-Substitution in $(Ga_{1-x}Mg_x)(Ga_{1-x}Ge_x)O_3$:Cr³+. ACS Appl. Mater. Interfaces **2022**, 14 (45), 51157–51164.
- (41) Toby, B. H.; Von Dreele, R. B. *GSAS-II*: The Genesis of a Modern Open-Source All Purpose Crystallography Software Package. *J. Appl. Crystallogr.* **2013**, *46* (2), 544–549.

- (42) Toby, B. H. EXPGUI, a Graphical User Interface for GSAS. J. Appl. Crystallogr. 2001, 34 (2), 210–213.
- (43) Momma, K.; Izumi, F. VESTA 3 for Three-Dimensional Visualization of Crystal, Volumetric and Morphology Data. J. Appl. Crystallogr. 2011, 44 (6), 1272–1276.
- (44) Hafner, J. Ab-initio Simulations of Materials Using VASP: Density-functional Theory and Beyond. J. Comput. Chem. 2008, 29 (13), 2044–2078.
- (45) Peverati, R.; Zhao, Y.; Truhlar, D. G. Generalized Gradient Approximation That Recovers the Second-Order Density-Gradient Expansion with Optimized Across-the-Board Performance. *J. Phys. Chem. Lett.* **2011**, 2 (16), 1991–1997.
- (46) Hariyani, S.; Duke, A. C.; Krauskopf, T.; Zeier, W. G.; Brgoch, J. The Effect of Rare-Earth Substitution on the Debye Temperature of Inorganic Phosphors. *Appl. Phys. Lett.* **2020**, *116* (5), No. 051901.
- (47) Ha, J.; Wang, Z.; Novitskaya, E.; Hirata, G. A.; Graeve, O. A.; Ong, S. P.; McKittrick, J. An Integrated First Principles and Experimental Investigation of the Relationship between Structural Rigidity and Quantum Efficiency in Phosphors for Solid State Lighting. *J. Lumin.* **2016**, *179*, 297–305.
- (48) Zhang, H.; Zhong, J.; Du, F.; Chen, L.; Zhang, X.; Mu, Z.; Zhao, W. Efficient and Thermally Stable Broad-Band Near-Infrared Emission in a KAlP₂O₇:Cr³⁺ Phosphor for Nondestructive Examination. ACS Appl. Mater. Interfaces **2022**, 14 (9), 11663–11671.
- (49) Makuła, P.; Pacia, M.; Macyk, W. How To Correctly Determine the Band Gap Energy of Modified Semiconductor Photocatalysts Based on UV–Vis Spectra. *J. Phys. Chem. Lett.* **2018**, 9 (23), 6814–6817.
- (50) Nie, W.; Li, Y.; Zuo, J.; Kong, Y.; Zou, W.; Chen, G.; Peng, J.; Du, F.; Han, L.; Ye, X. Cr³⁺ -Activated Na₃X₂Li₃F₁₂ (X = Al, Ga, or In) Garnet Phosphors with Broadband NIR Emission and High Luminescence Efficiency for Potential Biomedical Application. *J. Mater. Chem. C* **2021**, *9* (42), 15230–15241.
- (51) Sójka, M.; Zhong, J.; Brgoch, J. Developing Broadband Cr³⁺-Substituted Phosphor-Converted Near-Infrared Light Sources. *ACS Appl. Opt. Mater.* **2023**, *1* (6), 1138–1149.
- (52) Hariyani, S.; Sójka, M.; Setlur, A.; Brgoch, J. A Guide to Comprehensive Phosphor Discovery for Solid-State Lighting. *Nat. Rev. Mater.* **2023**, *8* (11), 759–775.
- (53) Hu, T.; Molokeev, M. S.; Xia, Z.; Zhang, Q. Aliovalent Substitution toward Reinforced Structural Rigidity in Ce³⁺ -Doped Garnet Phosphors Featuring Improved Performance. *J. Mater. Chem.* C **2019**, *7* (46), 14594–14600.
- (54) Wang, Y.; Ding, J.; Zhou, X.; Wang, Y. Promotion of Efficiency and Thermal Stability by Restraining Dynamic Energy Migration Based on the Highly Symmetric Rigid Structure in the N-UV Excitation Green Emission Garnet Phosphors. *Chem. Eng. J.* **2020**, 381, No. 122528.
- (55) Shannon, R. D. Revised Effective Ionic Radii and Systematic Studies of Interatomic Distances in Halides and Chalcogenides. *Acta Crystallogr., Sect. A* **1976**, 32 (5), 751–767.
- (56) Wang, S.; Pang, R.; Tan, T.; Wu, H.; Wang, Q.; Li, C.; Zhang, S.; Tan, T.; You, H.; Zhang, H. Achieving High Quantum Efficiency Broadband NIR Mg₄Ta₂O₉:Cr³⁺ Phosphor Through Lithium-Ion Compensation. *Adv. Mater.* **2023**, *35* (22), No. 2300124.
- (57) Ikemoto, I.; Ishii, K.; Kinoshita, S.; Kuroda, H.; Franco, M. A. A.; Thomas, J. M. X-Ray Photoelectron Spectroscopic Studies of CrO₂ and Some Related Chromium Compounds. *J. Solid State* **1976**, 17, 425–430, DOI: 10.1016/S0022-4596(76)80012-6.
- (58) Rajendran, V.; Fang, M. H.; Huang, W. T.; Majewska, N.; Lesniewski, T.; Mahlik, S.; Leniec, G.; Kaczmarek, S. M.; Pang, W. K.; Peterson, V. K.; Lu, K. M.; Chang, H.; Liu, R. S. Chromium Ion Pair Luminescence: A Strategy in Broadband near-Infrared Light-Emitting Diode Design. J. Am. Chem. Soc. 2021, 143 (45), 19058–19066.
- (59) Li, R.; Liu, Y.; Yuan, C.; Leniec, G.; Miao, L.; Sun, P.; Liu, Z.; Luo, Z.; Dong, R.; Jiang, J. Thermally Stable CaLu₂Mg₂Si₃O₁₂:Cr³⁺ Phosphors for NIR LEDs. *Adv. Opt. Mater.* **2021**, 9 (16), No. 2100388.

- (60) Nie, W.; Yao, L.; Chen, G.; Wu, S.; Liao, Z.; Han, L.; Ye, X. A Novel Cr³⁺ -Doped Lu₂CaMg₂Si₃O₁₂ Garnet Phosphor with Broadband Emission for Near-Infrared Applications. *Dalton Trans.* **2021**, *50* (24), 8446–8456.
- (61) Xie, J.; Tian, J.; Zhuang, W. Near-Infrared Lu-Ca₂ScZrGa₂GeO₁₂:Cr³⁺ Garnet Phosphor with Ultra-Broadband Emission for NIR LED Applications. *Inorg. Chem.* **2023**, *62* (27), 10772–10779.
- (62) Zeng, H.; Zhou, T.; Wang, L.; Xie, R.-J. Two-Site Occupation for Exploring Ultra-Broadband Near-Infrared Phosphor—Double-Perovskite La₂MgZrO₆:Cr³⁺. *Chem. Mater.* **2019**, 31 (14), 5245–5253
- (63) Yan, Y.; Shang, M.; Huang, S.; Wang, Y.; Sun, Y.; Dang, P.; Lin, J. Photoluminescence Properties of $AScSi_2O_6:Cr^{3+}$ (A = Na and Li) Phosphors with High Efficiency and Thermal Stability for Near-Infrared Phosphor-Converted Light-Emitting Diode Light Sources. ACS Appl. Mater. Interfaces 2022, 14 (6), 8179–8190.
- (64) Li, C.; Zhong, J.; Jiang, H.; Shi, P. Efficient and Thermally Stable Broadband Near-Infrared Emission in a Garnet Gd₃In₂Ga₃O₁₂:Cr³⁺ Phosphor. *Dalton Trans.* **2022**, *51* (43), 16757–16763.
- (65) Hou, D.; Lin, H.; Zhang, Y.; Li, J.-Y.; Li, H.; Dong, J.; Lin, Z.; Huang, R. A Broadband Near-Infrared Phosphor BaZrGe₃O₉:Cr³⁺: Luminescence and Application for Light-Emitting Diodes. *Inorg. Chem. Front.* **2021**, *8* (9), 2333–2340.
- (66) Ueda, J.; Dorenbos, P.; Bos, A. J. J.; Meijerink, A.; Tanabe, S. Insight into the Thermal Quenching Mechanism for $Y_3Al_5O_{12}$: Ce^{3+} through Thermoluminescence Excitation Spectroscopy. *J. Phys. Chem. C* **2015**, *119* (44), 25003–25008.
- (67) Ueda, J.; Aishima, K.; Tanabe, S. Temperature and Compositional Dependence of Optical and Optoelectronic Properties in Ce^{3+} Doped $Y_3Sc_2Al_{3-x}Ga_xO_{12}$ (X = 0, 1, 2, 3). *Opt. Mater.* **2013**, 35 (11), 1952–1957.
- (68) Lin, Q.; Wang, Q.; Liao, M.; Xiong, M.; Feng, X.; Zhang, X.; Dong, H.; Zhu, D.; Wu, F.; Mu, Z. Trivalent Chromium Ions Doped Fluorides with Both Broad Emission Bandwidth and Excellent Luminescence Thermal Stability. ACS Appl. Mater. Interfaces 2021, 13 (15), 18274–18282.
- (69) Song, E.; Ming, H.; Zhou, Y.; He, F.; Wu, J.; Xia, Z.; Zhang, Q. Cr³⁺ -Doped Sc-Based Fluoride Enabling Highly Efficient Near Infrared Luminescence: A Case Study of K₂NaScF₆:Cr³⁺. *Laser Photonics Rev.* **2021**, *15* (2), No. 2000410.
- (70) Yao, L.; Shao, Q.; Han, S.; Liang, C.; He, J.; Jiang, J. Enhancing Near-Infrared Photoluminescence Intensity and Spectral Properties in Yb³⁺ Codoped LiScP₂O₇:Cr³⁺. *Chem. Mater.* **2020**, 32 (6), 2430–2439.
- (71) Shao, Q.; Ding, H.; Yao, L.; Xu, J.; Liang, C.; Jiang, J. Photoluminescence Properties of a ScBO₃:Cr³⁺ Phosphor and Its Applications for Broadband near-Infrared LEDs. *RSC Adv.* **2018**, 8 (22), 12035–12042.
- (72) Huang, D.; Zhu, H.; Deng, Z.; Yang, H.; Hu, J.; Liang, S.; Chen, D.; Ma, E.; Guo, W. A Highly Efficient and Thermally Stable Broadband Cr³⁺ -Activated Double Borate Phosphor for Near-Infrared Light-Emitting Diodes. *J. Mater. Chem. C* **2021**, 9 (1), 164–172.
- (73) Liu, Y.; He, S.; Wu, D.; Dong, X.; Zhou, W. Broadband NIR Garnet Phosphors with Improved Thermal Stability via Energy Transfer. ACS Appl. Electron. Mater. 2022, 4 (2), 643–650.
- (74) Wu, Z.; Ouyang, G.; Shi, X.; Ma, Q.; Wan, G.; Qiao, Y. Absorption and Quantitative Characteristics of C-H Bond and O-H Bond of NIR. *Opt. Spectrosc.* **2014**, *117* (5), 703–709.